Astroparticle Physics 33 (2010) 69–74

Contents lists available at ScienceDirect

Astroparticle Physics

journal homepage: www.elsevier.com/locate/astropart

Disks in the sky: A reassessment of the WMAP "cold spot"

Ray Zhang, Dragan Huterer *

Department of Physics, University of Michigan, 450 Church St., Ann Arbor, MI 48109, United States

ARTICLE INFO

Article history:
Received 10 November 2009
Accepted 10 November 2009
Available online 26 November 2009

Keywords:
Cosmology
Cosmic microwave background

ABSTRACT

We reassess the evidence that WMAP temperature maps contain a statistically significant "cold spot" by repeating the analysis using simple circular top-hat (disk) weights, as well as Gaussian weights of varying width. Contrary to previous results that used Spherical Mexican Hat Wavelets, we find no significant signal at any scale when we compare the coldest spot from our sky to ones from simulated Gaussian random, isotropic maps. We trace this apparent discrepancy to the fact that WMAP cold spot's temperature profile just happens to favor the particular profile given by the wavelet. Since randomly generated maps typically do not exhibit this coincidence, we conclude that the original cold spot significance originated at least partly due to a fortuitous choice of using a particular basis of weight functions. We also examine significance of a more general measure that returns the most significant result among several choices of the weighting function, angular scale of the spot, and the statistics applied, and again find a null result.

1. Introduction

Cosmic microwave background (CMB) maps have been studied in detail during the last few years. These studies have been motivated by the remarkable full-sky high-resolution maps obtained by WMAP [1,2], and led to a variety of interesting and unexpected findings. Notably, various anomalies have been claimed pertaining to the alignment of largest modes in the CMB [3–9], the missing power on large angular scales [10–12], and the asymmetries in the distribution of power [13–16]. In the future, temperature maps obtained by the Planck experiment, and large-scale polarization information [17] may be key to determining the nature of the large-scale anomalies. For a review of the anomalies and attempts to explain them, see [18].

Several years ago, Ref. [19] reported an anomalously cold spot in the WMAP microwave signal: kurtosis of the distribution of spots (defined using Spherical Mexican Hat Wavelet weight functions) is unusually large on scales of about 5°, at <0.5% significance. The authors also noted that the result is driven by a cold spot in the southern hemisphere, at $(\ell, b) = (-57^\circ, 209^\circ)$. The finding has been confirmed and further investigated in Ref. [20], who found that an equally cold or colder spot of this size is expected in <1% of Gaussian random, isotropic skies, as well as Refs. [21–24,20,25–28], some of whom also studied the spot's morphology. The plot further thickened when Rudnick et al. [29] claimed that there is a corresponding cold spot (underdensity in galaxy counts) – in the NVSS radio survey, and at roughly the same location as the CMB cold spot; however, this particular claim was shown by Ref. [30] to be an artifact of the *a posteriori* statistics and the particular way NVSS data had been analyzed. Nevertheless, the CMB cold spot remains a much-studied topic and the source of investigations of whether exotic physics could be the cause.

Perhaps surprisingly, nearly all of the works so far considered searches for the cold spot using the same basis functions – Spherical Mexican Hat Wavelets (though with a few exceptions – Ref. [27] used needlets, while [25,28] used the scaling indices). The only variation in the different analyses was in the choice of the statistics that was applied to the wavelet-based weights.

Here we set out to check the evidence for the cold spot using different, and arguably simpler, set of weight functions. We reassess evidence for the "cold spot" using circular top-hat weights (i.e. disks) of arbitrary radius R. We do so in order to verify findings that relied on wavelets, and more generally to investigate the robustness of the signal. We also check results using simple Gaussian weights, finding results consistent with those with the disks. We then investigate the source of this apparent discrepancy with all of the previous work that used wavelets, and find that the cause of the discrepancy is the specific temperature profile of the cold spot which just happens to favor the profile of the Spherical Mexican Hat Wavelet. In addition to the choice of the spots' weight function, the original claim refers to the angular size of the spot of $\sim 5^\circ$ that is also chosen *a posteriori*. We investigate the effect of these choices by defining a "superstatistic" measure that combines several previously considered statistical measures of coldness and the associated choices of the spot size and weight functions, and find that the claimed spot (or any other spot in our sky) is not unusually significant using this new measure.

* Corresponding author. Tel.: +1 734 615 3289.
E-mail addresses: rayzhang@umich.edu (R. Zhang), huterer@umich.edu (D. Huterer).

0927-6505/$ - see front matter © 2009 Elsevier B.V. All rights reserved.
doi:10.1016/j.astropartphys.2009.11.005

2. Statistics and maps

2.1. Weight statistics

The top-hat weights are familiar from structure formation (where they are used in the definition of the amplitude of mass fluctuations over some scale R, for example) and effectively represent another statistic to study the cold spot. We define the disk top-hat weight of radius R as

$$D(r) \equiv A_{\rm disk}(R)[\Theta(r) - \Theta(r-R)], \tag{1}$$

where $\Theta(x)$ is a Heaviside step function and $A_{\rm disk}(R) = (2\pi(1-\cos(R)))^{-1/2}$ is defined so that

$$\int_0^\pi D(r)^2\, d\Omega = 1. \tag{2}$$

Note however, that the normalization $A_{\rm disk}(R)$ is unimportant for finding the coldest spot since we only do relative comparisons of temperatures in disks on the sky. The top-hat-weighted temperature coefficients are given by

$$T_{\rm disk}(\hat{r};R) = \int d\Omega' T(\hat{r}') D(\alpha;R), \tag{3}$$

where $\hat{r} = (\theta,\phi)$ is the location of a given spot, $\hat{r}' = (\theta',\phi')$ is the dummy location on the sky whose temperature we integrate over, and $\alpha = \arccos(\hat{r}\cdot\hat{r}')$ is the angle between the two directions.

The Gaussian weights that we use are defined equivalently. The weight functions are

$$G(r) \equiv A_{\rm Gauss}(R)\exp\left(-4\ln 2\frac{r^2}{R^2}\right), \tag{4}$$

so that the full-width at half-maximum of the distribution is equal to R. The weighted temperatures are given by

$$T_{\rm Gauss}(\hat{r};R) = \int d\Omega' T(\hat{r}') G(\alpha;R). \tag{5}$$

Finally, the corresponding procedure applied to the wavelets is as follows [31,32]. The Spherical Mexican Hat Wavelets are defined as

$$\Psi(\theta;R) = A_{\rm wav}(R)\left(1+\left(\frac{y}{2}\right)^2\right)^2\left(2-\left(\frac{y}{R}\right)^2\right)\exp\left(\frac{-y^2}{2R^2}\right), \tag{6}$$

where $y \equiv 2\tan(\theta/2)$ and

$$A_{\rm wav}(R) = \left[2\pi R^2\left(1+\frac{R^2}{2}+\frac{R^4}{4}\right)\right]^{-1/2}, \tag{7}$$

so that $\int d\Omega\, \Psi^2(\theta;R) = 1$ over the whole sky.

We can now define the continuous wavelet transform stereographically projected over the sphere with respect to $\Psi(\theta;R)$, with T being the CMB temperature:

$$T_{\rm wav}(\vec{x};R) = \int d\Omega' T(\vec{x}+\vec{\mu}')\Psi(\theta';R), \tag{8}$$

where $\vec{x} \to (\theta,\phi)$ and $\vec{\mu}' \to (\theta',\phi')$ are the stereographic projections to the sphere of the center of the spot and the dummy location, respectively, and are given by

$$\vec{x} = 2\tan\frac{\theta}{2}(\cos\phi, \sin\phi), \tag{9}$$

$$\vec{\mu}' = 2\tan\frac{\theta'}{2}(\cos\phi', \sin\phi'), \tag{10}$$

see Ref. [32] for details. To work in terms of purely spherical coordinates, we center the spot location to the north pole of the sphere, and rewrite the above as

$$T_{\rm wav}(\hat{r};R) = \int d\Omega' T(\hat{r}')\Psi(\alpha;R), \tag{11}$$

where $M(\hat{r}')$ is the mask, defined to be 1 for pixels within the mask and 0 for those outside of it. As the wavelet is effectively zero for α values greater than ~ 4 times the radius, we can carry out the integral by using the Healpix command `query_disc` to find all pixels within a circle of that radius from the wavelet center.

To account for the masked parts of the sky, at each spot location $\hat{r}$ we first calculate the "occupancy fraction"

$$N(\hat{r};R) = \int d\Omega' M(\hat{r}')\Psi^2(\theta;R). \tag{12}$$

We only include results for spot locations $\hat{r}$ for which $N(\hat{r};R) > 0.95$. Additionally, we do not include individual *pixels* that have $M(\hat{r}') < 0.9$ in order to limit biases due to masking (partially masked pixels come about after degrading maps to a lower resolution). As discussed further below, we tested our procedures by using a higher occupancy fraction and found consistent results.

2.2. Maps

We use WMAPs five-year maps in our analysis [33]. Following Ref. [19], the fiducial map we use is the coadded foreground-cleaned map

$$T = \frac{\sum_{r=3}^{10} T_r(i) w_r(i)}{\sum_{r=3}^{10} w_r(i)}, \tag{13}$$

where T is the coadded temperature, determined from the weighted sum of temperatures T_r of each individual radiometer $r \in \{Q1, Q2, V1, V2, W1, W2, W3, W4\}$, divided by the total weight. The weights at each pixel for each radiometer are $w_r(i) = N_r(i)/\sigma_r^2$, where $N_r(i)$ are the number of effective observations at the pixel, and σ_r is the noise dispersion for the given receiver.

This coadding was performed on maps at resolution of $N_{\rm side} = 512$ ($\sim 8'$), then the KQ75 mask was applied. As mentioned earlier, spots with more than 5% of the weighted area masked ($N(\hat{r};R) > 0.95$) were not used.

The locations of centroids of spots are chosen to be centers of pixels in $N_{\rm side} = 32$ resolution; therefore, we examine $N_{\rm pix} = 12N_{\rm side}^2 \sim 12,000$ spots on the sky. In order to calculate the spots' weighted temperatures, however, we analyze the coadded map at the $N_{\rm side} = 128$ ($\sim 0.5^\circ$) resolution, which is sufficiently high to lead to converged results for $R \gtrsim 2^\circ$ spots, yet sufficiently low to be numerically feasible.

The results of our analysis were then compared to 10,000 randomly generated Gaussian full-sky maps, with the same methodology applied. The skies have been generated using the Healpix facility `synfast`, and used as input the power spectrum determined in the WMAP 5-year analysis [34]. The maps were then smoothed by a Gaussian with FWHM = 1° to match the WMAP procedure.

2.3. Significance statistics

The principal statistic that we use is the temperature of the coldest spot divided by the standard deviation of the distribution of all spots

$$S_{\rm disk}(\hat{r};R) \equiv \frac{T_{\rm disk}^{\rm coldest}(\hat{r},R)}{\sigma_{\rm disk}(R)} \tag{14}$$

and equivalently for the Gaussian weights and the wavelets. Here $\sigma_{\rm disk}(R)$ is the standard deviation of the distribution of all spots in a given map, while $T_{\rm disk}^{\rm coldest}(R)$ is the coldest spot in the distribution. Note that the distribution of spot temperatures is not Gaussian as we noted earlier, but this is irrelevant for us; we scale T by σ in

Eq. (14) in order to account for small (∼10%) differences in the overall level of power in spots of characteristic size R in the different maps – in effect, $\sigma_{\rm disk}(R)$ provides units in which to best report the coldest temperature.

Computing the significance of our statistic $S_{\rm disk}(\hat{r};R)$ is then in principle straightforward: we compare it to values obtained from simulated Gaussian random maps and rank-order it; the rank gives the probability.

In addition to the cold spot significance, we follow Refs. [19,22] and consider the kurtosis of spots in a given map. The kurtosis is simply related to the fourth moment of the distribution of the spots

$$K_{\rm disk}(R) \equiv \frac{1}{N_{\rm spots}} \frac{\sum_{i=1}^{N_{\rm spots}} T_{\rm disk}(\hat{r}_i,R)^4}{\sigma_{\rm disk}(R)^4} - 3 \qquad (15)$$

and equivalently for the Gaussian weights and the wavelets.

3. Results

3.1. Wavelet weighted spot

We first make sure that we reproduce the cold spot results of [19,22]. For Spherical Mexican Hat Wavelets with $R = 5^\circ$, we find the center of the coldest spot in the five-year combined cleaned map, is at coordinates $(\ell, b) = (-57.7^\circ, 209.3^\circ)$ (corresponding to spherical coordinates $(\theta, \phi) = (147.7^\circ, 209.3^\circ)$). In general agreement with the Ref. [35] results, we find that only $(0.99 \pm 0.10)\%$ of simulated statistically isotropic, Gaussian random maps exhibit a more significant cold spot (i.e. a more negative value of $S_{\rm wav}^{\rm coldest}(R)$) for this value of R. Here and throughout, the error bars account for the finite number of $(N = 10,000)$ simulated maps; we quote the standard margin of error which, for a fraction p of a total of N events, is given as $\sigma(p) = \sqrt{p(1-p)/N}$. Moreover, we confirm that while the variance and skewness of the distribution of $S_{\rm wav}^{\rm coldest}(R)$ from synthetic maps, the kurtosis at $R = 5^\circ$ is high at the $(1.44 \pm 0.12)\%$ confidence.

Reporting the significance only for the $R = 5^\circ$ may be unfair, however. To address this, we consider the range $2^\circ \leqslant R \leqslant 8^\circ$ in steps of 0.5° (the lower bound is set to correspond to spots significantly larger than smoothing of the maps of roughly 1°). The significances of these results are given as black lines in the two panels of Fig. 1.[1] The significance of the wavelet-determined cold spot peaks around $R = 5$–6°, while the kurtosis is significant in the range $3^\circ \leqslant R \leqslant 5^\circ$.

3.2. Disk and Gaussian weighted spot

We now repeat the same analysis with the circular weights. First we confirm that the coldest disk-weighted spot in the co-added smoothed Q–V–W map is at nearly the same location as the wavelet-weighted spot, at $(\ell, b) = (-57.4, 208.0)$. The result is similar in the foreground cleaned Q–V–W map. However, the disk-weighted spot is not unusually cold: at all scales R between 2° and 8°, the statistic $S_{\rm disk}^{\rm coldest}(R)$ is not unusually low relative to expectations from Gaussian random maps; see the left panel of Fig. 1. We find the same results for the kurtosis of the distribution of $S_{\rm disk}(\hat{r};R)$ – as shown in the right panel of Fig. 1 these distributions fall well within the expectation on all scales we examined.

Surprised by these results, we have repeated the same tests with Gaussian weighting, where the full-width half-maximum (FWHM) of the Gaussian weight has been set equal to the scale R; this way we ensure that a large fraction (about 94%) of the weight is applied within the radius R. The results are similar as for the disks in that they are not significant; see again Fig. 1. In particular, the coldest spot is most significant at $R = 4 - 5^\circ$, but even there only at the $1 - \sigma$ (25%) level, while the kurtosis is not significantly large or small at any scale.

3.3. The density profile of the cold spot

The question is obvious: Why was the cold spot so significant for wavelets, but not so much for disks? To address this, we show the disk and wavelet weights, together with the azimuthally-averaged CMB temperature profile, as a function of radial distance from the (wavelet-found) center of the cold spot in the left panel of Fig. 2. In the right panel, we show contribution to the weighted temperature using disks and wavelets, as well as the cumulative difference between the two. This figure shows the case of $R = 5^\circ$ which approximately maximizes significance of the wavelet-based cold spot.

The azimuthally-averaged density profile of the temperature is about equally distributed between zero and 5° (that is, the blue area in the right panel is about the same as the red one up to 5°). However, at distance beyond the edge of the disk of 5°, the wavelet accumulates more weight as seen in the right panel. The reason is shown with the curve labeled "averaged CMB temperature" in the left panel: the CMB profile goes from negative to positive with increasing radius from the center of the (wavelet-based) cold spot, precisely favoring the wavelet profile that has roughly the opposite behavior.

What is the likelihood of this conspiracy that the temperature profile of the coldest spot mimics the shape of the wavelet? Using Gaussian random maps, we estimate the likelihood that a given map has the wavelet-determined cold spot is more significant than the disk-determined cold spot by *at least* as much as in WMAP where $\left|S_{\rm wav}^{\rm coldest}(R) - S_{\rm circ}^{\rm coldest}\right| = 1.5$. We find that the wavelets are more significant that the disks by at least this margin in only $(1.89 \pm 0.13)\%$ of the random maps (while the disks are as or more significant in only $(1.96 \pm 0.14)\%$ cases). From this, we conclude that typical Gaussian random CMB maps do not show increased significance of the wavelet-determined cold spot, relative to the disk-determined one, to the same extent as our sky does (see Table 1).

3.4. Robustness

We have tried varying a number of details, with the following results:

- In addition to the coadded *foreground cleaned* Q + V + W map, we also used the coadded Q + V + W map, the coadded V + W map, and the coadded foreground cleaned V + W maps available from WMAP. All of the significances are very close to the foreground QVW map value; we have checked that smaller scales (1–1.5°), which were not in the range we presented in the final analysis, would be somewhat discrepant; this is not surprising given that the maps are smoothed to 1°.
- To test the effects of the resolution of the map, we vary the resolution from $N_{\rm side} = 128$ ($\sim 0.5^\circ$ pixels) to $N_{\rm side} = 32$ ($\sim 2^\circ$ pixels), with 16 times fewer pixels. We again find consistent results except at small scales, $R < 2^\circ$, which makes sense since pixelization is expected to play a role only when pixel size becomes comparable to the spot scale R.
- To ensure that our finite step size has not accidentally overlooked a cold spot, we refine the resolution in our search for the coldest spot in WMAP by querying at *every* pixel in an

[1] These tests are computing-intensive, and we were forced to compare to simulated maps at $N_{\rm side} = 32$ (rather than $N_{\rm side} = 128$) for wavelets for $6.5^\circ \leqslant R \leqslant 8^\circ$; we have checked at lower values of R that the results at the two resolutions are in good agreement.

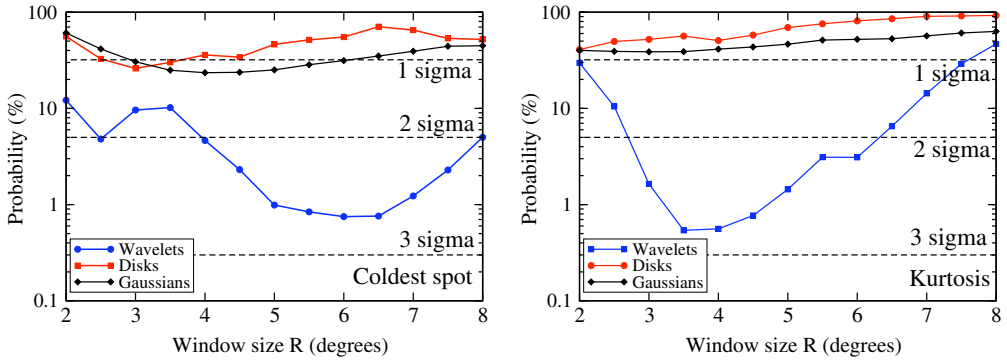

Fig. 1. Significance in "sigmas" of the cold spot temperature $S^{\text{coldest}}(R)$ (left panel) and kurtosis of the distribution of $S(R)$ (right panel) for the three choices of weights that we have examined: disks (red), Gaussians (black) and wavelets (blue). Here 1σ means <32% likely, 2σ means <5% likely, and 3σ corresponds to <0.3%. Note that the scale R, shown on the x-axis, is defined separately for each choice of the weighting function so that the corresponding fair comparison can be made; see text for details. The results show that only the wavelet-based temperature cold spot and kurtosis deviate significantly from the Gaussian random expectation, and that the disk or Gaussian ones do not. (For interpretation of the references to colour in this figure legend, the reader is referred to the web version of this article.)

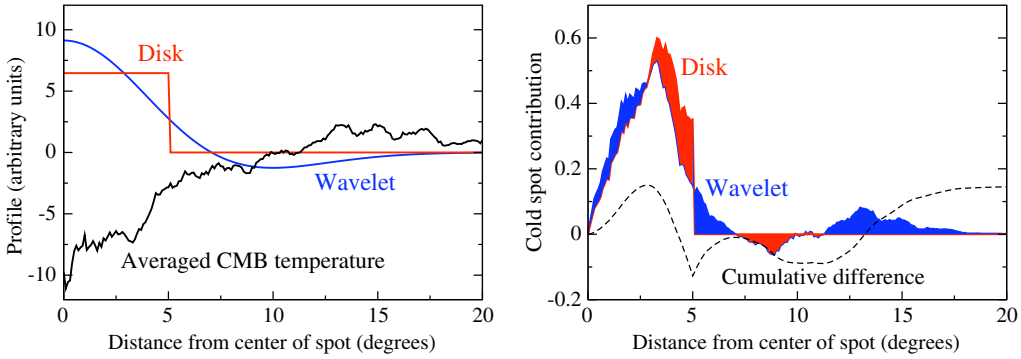

Fig. 2. Left panel: disk and wavelet weights, together with the azimuthally-averaged CMB temperature profile as a function of radial distance from the (wavelet-found) center of the cold spot. Right panel: contribution to the weighted temperature using disks and wavelets; the blue (red) shaded areas show the difference by which wavelets (disks) dominate in the given ranges of distance, while the dashed line shows the cumulative difference between the two. Note that all lines in both panels have arbitrary normalization, although the disk and wavelet lines are consistently compared using their fiducial normalizations from the text. (For interpretation of the references to colour in this figure legend, the reader is referred to the web version of this article.)

Table 1
Statistics and its significance for coldest spot and kurtosis of spots, evaluated on scale $R = 5^\circ$, for the three weights we considered. For the coldest spot, the statistics is S, defined in Eq. (14), while for kurtosis, the statistic is just its value, defined in Eq. (15). The error bars are Poisson and reflect the finite number of the simulated Gaussian random maps to which we compared WMAP. The results are robust to variation in the choice of the WMAP map, or radius R, as discussed in the text.

	Cold spot statistic ($R = 5^\circ$)			Kurtosis statistic ($R = 5^\circ$)		
	Wavelet	Disk	Gaussian	Wavelet	Disk	Gaussian
Value of statistic	−3.21	−4.54	−3.52	0.58	−0.23	−0.06
Significance in %	0.99 ± 0.10	46.3 ± 0.5	25.1 ± 0.4	1.44 ± 0.12	69.3 ± 0.5	46.5 ± 0.5

$N_{\text{side}} = 512$ map within 3° of the center of the reported cold spot; this stepping size is effectively ∼256 times higher than before. While an increase in the temperature of the cold spot is entirely expected, we find that this increase is small enough not to appreciably change the significance results for all three choices of the weight function.

- To test our prescription for dealing with partially masked spots, where we only analyze spots that have the "occupancy fraction" $N(\hat{r}; R) > 0.95$ (see Eq. (12)), we repeat the analysis with the minimum occupancy number of 0.98. While the resulting *number* of spots retained in the analysis is now much smaller, decreasing by between tens of percent (for spots at $R = 2^\circ$) to about a factor of 10 (for $R = 8^\circ$ disks), we find results generally consistent with our fiducial case: the statistic S and kurtosis calculated using the wavelet weights are significant, while the same statistics calculated using the disk and Gaussian weights are not.

3.5. More general tests

It is clear that *a posteriori* choices were made in the original claims for the existence of the cold spot – in addition to the choice of the weighting function (which is the principal subject of this paper), the moment of the distribution of spots (kurtosis) and spot scale (5°) have been called out *after* noticing that they are unusual.[2] In contrast, variance and skewness of the spot distribution, or kurtosis and scales larger or smaller than ∼5°, do not show departures from expectations based on Gaussian random isotropic maps, as we have checked as well.

[2] While observation of some of the other anomalies mentioned in the introduction was technically also *a posteriori*, those anomalies had to do with special scales (e.g. largest observable scales on the sky) or directions (e.g. the ecliptic, which the telescope pointings preferentially avoid). In contrast, there appears to be nothing special about kurtosis of the spot distribution, or scales of ∼5°.

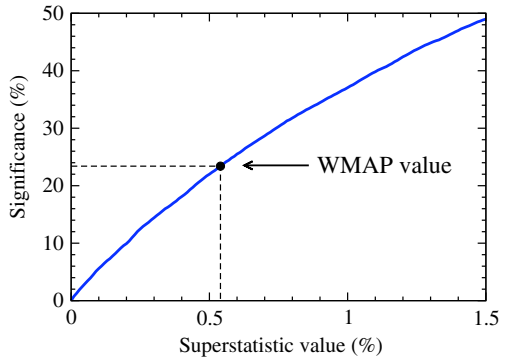

Fig. 3. Significance of the superstatistic $\mathscr{S}_{\rm super}$, defined in Eq. (16), as a function of its value. The line shows results calibrated from our simulated maps, while the point denotes the value (and the unremarkable significance) from WMAP.

We have investigated how results change with more general tests as follows. We have formed a "superstatistic" defined as maximum significance of either variance, skewness, kurtosis, or coldness (the last two being defined earlier in this section) over any scale R or weight function set W

$$\mathscr{S}_{\rm super} \equiv \max_{R,W,{\rm Stat}} \{P({\rm Stat}_W(R))\} \tag{16}$$

where[3]

$$\begin{aligned} &R \in \{2^\circ, 2.5^\circ, \ldots, 8^\circ\} \\ &W \in \{{\rm wavelet}, {\rm disk}, {\rm Gaussian}\} \\ &{\rm Stat} \in \{{\rm Variance}, {\rm Skewness}, {\rm Kurtosis}, S\} \end{aligned} \tag{17}$$

and where each probability P was individually calculated relative to Gaussian random isotropic maps as described earlier. [The S and kurtosis statistics have been defined in Eqs. (14) and (15), while the variance and skewness are defined analogously to kurtosis.] Note that we define P to capture the possibility that the statistics in question is either small or large relative to expectation; in other words, we adopt the minimum of r and $(100\% - r)$, where r is the rank of the statistics relative to simulated maps.

We find that the value of the $\mathscr{S}_{\rm super}$ statistic for the WMAP cleaned QVW map is 0.54%, and this value is attained by the kurtosis statistic $S_{\rm wavelet}$ at scale $R = 3.5^\circ$. However, this value is not too unusual: we find that 23% of the Gaussian random skies have a smaller value of $\mathscr{S}_{\rm super}$; see Fig. 3.

To test the robustness of this result, we consider an alternative, more restricted, definition of the superstatistic where only the wavelet weights are considered, but where we still varying scale R and statistic Stat; see Eq. (17). Here we effectively assume that, for whatever reason, wavelets are the preferred weight functions to be used, but we still seek to avoid the *a posteriori* choices of the scale and statistics. The new superstatistic is again not statistically significant; we find that 15% of Gaussian random skies show greater significance.

Thus, superstatistic results confirm our earlier conclusion that less *a posteriori* tests do not indicate a statistically significant cold spot in the WMAP data.

[3] For wavelets with $6.5^\circ \leqslant R \leqslant 8^\circ$ the calculations at $N_{\rm side} = 128$ were unfeasible due to the large number of pixels to keep track of. While we have checked that $N_{\rm side} = 32$ wavelet results are similar to $N_{\rm side} = 128$ at $R < 6.5^\circ$, and show no significant results at larger scales, for consistency we decided to quote the superstatistic results at $N_{\rm side} = 128$ and consider the $2^\circ \leqslant R \leqslant 6.5^\circ$ scales for the wavelets, and $2^\circ \leqslant R \leqslant 8^\circ$ for the disks and Gaussians.

4. Conclusions

The "cold spot", together with low power at large angles, multipole alignments, north–south power asymmetry, has been one of the most studied anomalies in WMAP CMB temperature maps. So far there have been no compelling proposals, cosmological or systematic, that would explain existence of the claimed cold spot, which is perhaps not surprising given that neither its radius ($\sim 5^\circ$) nor its direction in the sky are particularly special.

In this paper, we have investigated evidence for the cold spot. While we confirmed its high statistical significance using the wavelet basis of weight functions, we did not confirm the existence using the disk top-hat, or Gaussian, weights. The cold spot is indeed at the same location in WMAP maps with the latter two bases, but it is not significant when compared to expectation based on Gaussian random, isotropic skies.

We traced the apparent inconsistency to the fact that the radial temperature profile around the cold spot center is such that it favors the wavelet profile; see Fig. 2. This is a chance event, since only 5% of the Gaussian random, isotropic skies exhibit equal or more significant discrepancy in favor of the wavelets. Moreover, we found that the result is insensitive to the choice of the map or the statistic used for the cold spot.

Motivated by these findings, we also examined significance of a more general measure – which we called the "superstatistic" – that combines the various choices of the weighting function, spot size, and statistics, and returns the most significant choice consistently for each map. We again find a null result; the WMAP superstatistic is low only at $\sim$20% level relative to Gaussian random and isotropic simulated maps.

Therefore, we find no compelling evidence for the anomalously cold spot in WMAP at scales between 2° and 8°. The existing evidence apparently hinges on the particular choice of the weight functions to define the spot (Spherical Mexican Hat Wavelets) and their scale ($R \sim 5^\circ$). While our conclusion may sound like a depressing null result, we are upbeat about future tests with WMAP (and soon, Planck) to uncover and test unexpected features and anomalies.

Acknowledgements

We acknowledge use of the HEALPix [36] package, and also the Legacy Archive for Microwave Background Data Analysis (LAMBDA). We thank Christoph Räth and Patricio Vielva for useful communications. D.H. is supported by the DOE OJI Grant under Contract DE-FG02-95ER40899, NSF under Contract AST-0807564, and NASA under Contract NNX09AC89G. He thanks the Aspen Center for Physics for hospitality while this work was nearing completion.

References

[1] C.L. Bennett et al., First year Wilkinson microwave anisotropy probe (WMAP) observations: preliminary maps and basic results, ApJS 148 (2003) 1–27.
[2] D. Spergel et al., Wilkinson microwave anisotropy probe (WMAP) three year results: implications for cosmology, Astrophys. J. Suppl. 170, arXiv:astro-ph/0603449.
[3] M. Tegmark, A. de Oliveira-Costa, A.J. Hamilton, High resolution foreground cleaned CMB map from WMAP, Phys. Rev. D 68 (12) (2003) 123523.
[4] A. de Oliveira-Costa, M. Tegmark, M. Zaldarriaga, A. Hamilton, The significance of the largest scale cmb fluctuations in wmap, Phys. Rev. D D69 (2004) 063516. arXiv:astro-ph/0307282.
[5] C.J. Copi, D. Huterer, G.D. Starkman, Multipole vectors: a new representation of the CMB sky and evidence for statistical anisotropy or non-Gaussianity at $2 \leqslant \ell \leqslant 8$, Phys. Rev. D 70 (2004) 043515.
[6] D.J. Schwarz, G.D. Starkman, D. Huterer, C.J. Copi, Is the low-l microwave background cosmic?, Phys Rev. Lett. 93 (2004) 221301. arXiv:astro-ph/0403353.
[7] K. Land, J. Magueijo, The axis of evil, Phys. Rev. Lett. 95 (2005) 071301.

[8] C.J. Copi, D. Huterer, D.J. Schwarz, G.D. Starkman, On the large-angle anomalies of the microwave sky, Mon. Not. Roy. Astron. Soc. 367 (2006) 79–102. arXiv:astro-ph/0508047.
[9] L.R. Abramo, A. Bernui, I.S. Ferreira, T. Villela, C.A. Wuensche, Alignment tests for low CMB multipoles, Phys. Rev. D 74 (2006) 063506. arXiv:astro-ph/0604346.
[10] D.N. Spergel et al., First year Wilkinson microwave anisotropy probe (wmap) observations: determination of cosmological parameters, ApJS 148 (2003) 175. arXiv:astro-ph/0302209.
[11] C.J. Copi, D. Huterer, D.J. Schwarz, G.D. Starkman, Uncorrelated universe: statistical anisotropy and the vanishing angular correlation function in WMAP years 1 3, Phys. Rev. D 75 (2) (2007) 023507. arXiv:astro-ph/0605135.
[12] C.J. Copi, D. Huterer, D.J. Schwarz, G.D. Starkman, No large-angle correlations on the non-galactic microwave sky, arXiv:0808.3767.
[13] H.K. Eriksen, F.K. Hansen, A.J. Banday, K.M. Górski, P.B. Lilje, Asymmetries in the cmb anisotropy field, ApJ 605 (2004) 14–20. arXiv:astro-ph/0307507.
[14] F.K. Hansen, P. Cabella, D. Marinucci, N. Vittorio, Asymmetries in the local curvature of the wmap data, ApJ 607 (2004) L67–L70. arXiv:astro-ph/0402396.
[15] A. Bernui, T. Villela, C.A. Wuensche, R. Leonardi, I. Ferreira, On the cmb large-scales angular correlations, Astron. Astrophys. 454 (2006) 409–414. arXiv:astro-ph/0601593.
[16] A. Hajian, Analysis of the apparent lack of power in the cosmic microwave background anisotropy at large angular scales, arXiv:astro-ph/0702723.
[17] C. Dvorkin, H.V. Peiris, W. Hu, Testable polarization predictions for models of CMB isotropy anomalies, Phys. Rev. D D77 (2008) 063008. arXiv:0711.2321.
[18] D. Huterer, Mysteries on universe's largest observable scales, New Astron. Rev. 50 (2006) 868–874. arXiv:astro-ph/0608318.
[19] P. Vielva, E. Martinez-Gonzalez, R.B. Barreiro, J.L. Sanz, L. Cayón, Detection of non-Gaussianity in the wmap 1-year data using spherical wavelets, ApJ 609 (2004) 22–34. arXiv:astro-ph/0310273.
[20] M. Cruz, M. Tucci, E. Martinez-Gonzalez, P. Vielva, The non-Gaussian cold spot in WMAP: significance, morphology and foreground contribution, Mon. Not. Roy. Astron. Soc. 369 (2006) 57–67. arXiv:astro-ph/0601427.
[21] P. Mukherjee, Y. Wang, Wavelets and wmap non-Gaussianity, ApJ 613 (2004) 51–60. arXiv:astro-ph/0402602.
[22] M. Cruz, E. Martinez-Gonzalez, P. Vielva, L. Cayón, Detection of a non-Gaussian spot in wmap, MNRAS 356 (2005) 29–40. arXiv:astro-ph/0405341.
[23] J.D. McEwen, M.P. Hobson, A.N. Lasenby, D.J. Mortlock, A 6 sigma detection of non-Gaussianity in the wmap 1-year data using directional spherical wavelets, MNRAS 359 (2005) 1583–1596. arXiv:astro-ph/0406604.
[24] L. Cayón, J. Jin, A. Treaster, Higher Criticism statistic: detecting and identifying non-Gaussianity in the WMAP first-year data, MNRAS 362 (2005) 826–832. arXiv:astro-ph/0507246.
[25] C. Räth, P. Schuecker, A.J. Banday, A scaling index analysis of the Wilkinson microwave anisotropy probe three-year data: signatures of non-Gaussianities and asymmetries in the cosmic microwave background, Mon. Not. Roy. Astron. Soc. 380 (2007) 466–478, doi:10.1111/j.1365-2966.2007.12113.x.
[26] P.D. Naselsky et al., The mystery of the WMAP cold spot, arXiv:0712.1118.
[27] D. Pietrobon et al., Needlet detection of features in WMAP CMB sky and the impact on anisotropies and hemispherical asymmetries, Phys. Rev. D 78 (2008) 103504. arXiv:0809.0010.
[28] G. Rossmanith, C. Raeth, A.J. Banday, G. Morfill, Non-Gaussian signatures in the five-year WMAP data as identified with isotropic scaling indices, arXiv:0905.2854.
[29] L. Rudnick, S. Brown, L.R. Williams, Extragalactic radio sources and the WMAP cold spot, ApJ 671 (2007) 40–44. arXiv:0704.0908.
[30] K.M. Smith, D. Huterer, No evidence for the cold spot in the NVSS radio survey, arXiv:0805.2751.
[31] L. Cayon et al., Spherical mexican hat wavelet: an application to detect non-Gaussianity in the COBE-DMR maps, Mon. Not. Roy. Astron. Soc. 326 (2001) 1243. arXiv:astro-ph/0105111.
[32] E. Martinez-Gonzalez, J.E. Gallegos, F. Argueso, L. Cayon, J.L. Sanz, The performance of spherical wavelets to detect non-Gaussianity in the CMB sky, Mon. Not. Roy. Astron. Soc. 336 (2002) 22. arXiv:astro-ph/0111284.
[33] G. Hinshaw et al., Five-year Wilkinson microwave anisotropy probe (WMAP) observations: data processing, sky maps, & basic results, Astrophys. J. Suppl. 180 (2009) 225–245. arXiv:0803.0732.
[34] M.R. Nolta et al., Five-year Wilkinson microwave anisotropy probe (WMAP) observations: angular power spectra, Astrophys. J. Suppl. 180 (2009) 296–305. arXiv:0803.0593.
[35] M. Cruz, L. Cayon, E. Martinez-Gonzalez, P. Vielva, J. Jin, The non-Gaussian cold spot in the 3-year wmap data, Astrophys. J. 655 (2007) 11–20. arXiv:astro-ph/0603859.
[36] K.M. Górski, E. Hivon, A.J. Banday, B.D. Wandelt, F.K. Hansen, M. Reinecke, M. Bartelmann, HEALPix: a framework for high-resolution discretization and fast analysis of data distributed on the sphere, ApJ 622 (2005) 759–771.